




Equivalent Circuit Element Calculation of Gapped Multiwinding Inductors

Journal Article

Author(s):

[Ewald, Thomas](#) ; [Schlesinger, Richard](#) ; [Agner, Jan P.](#); [Biela, Jürgen](#) 

Publication date:

2023-05

Permanent link:

<https://doi.org/10.3929/ethz-b-000580484>

Rights / license:

[In Copyright - Non-Commercial Use Permitted](#)

Originally published in:

IEEJ Journal of Industry Applications 12(3), <https://doi.org/10.1541/ieejia.22007563>

Equivalent Circuit Element Calculation of Gapped Multiwinding Inductors

Thomas Ewald*^{a)} Non-member, Richard Schlesinger* Non-member
 Jan P. Agner* Non-member, Jürgen Biela* Non-member

Accurate and fast models of the equivalent circuit (EC) elements of gapped multiwinding inductors are essential for the design of galvanically isolated converters, such as Flyback and LLC converters. Typically, the EC elements are acquired from measurements or time-consuming FEM simulations, both of which are disadvantageous for optimizing the design of the magnetic device. This paper proposes a multiwinding magnetic device EC that exclusively uses the impedance matrix elements, i.e., self- and mutual impedances. The advantage of the impedance matrix equivalent circuit (IMEC) is that self- and mutual impedances are directly measurable. Furthermore, the paper presents an analytical 2D magnetic field model to calculate the EC elements. It is quantitatively confirmed that frequency significantly affects the resistances and the inductances of magnetically coupled windings. In particular, eddy currents in windings induced by the fringing field of the air gap play a role besides the well known skin and proximity effect. The proposed model accurately considers all these effects in foil, Litz, and round wire conductors. The model is verified using FEM simulations and measurements.

Keywords: Magnetic components, multiwinding inductor, coupled inductor, air gap fringing field, magnetic field, equivalent circuits

1. Introduction

Gapped multiwinding inductors are essential components in many power electronic converters such as Flyback converters⁽²⁾ and LLC converters⁽³⁾⁽⁴⁾. In multiwinding inductors, the elements of the impedance matrix – i.e. self- and mutual impedances – are significantly influenced by the fringing field of the air gap⁽¹⁾⁽⁵⁾. However, this impact of the air gap field has drawn little attention in literature in contrary to the well-described skin and proximity effect, even though the air gap fringing field induced eddy currents in the windings in vicinity to the air gap can be significant. Open-circuited windings close to the air gap are equally prone to this influence as short-circuited windings and windings under load. Thus, the air gap field induced eddy currents affect the self impedance of other magnetically coupled windings as well as their mutual impedances. In particular, eddy currents induced by the air gap field increase the winding losses and shield the rest of the core window from the air gap field by generating a counteracting magnetic field with increasing frequency⁽⁶⁾. This shielding effect leads to a drop in magnetic energy and hence, inductance⁽⁷⁾. The shielding effect is most pronounced with foil windings in vicinity to the air gap of the core. As the air gap field influences self- and mutual impedances, it needs to be taken into account when designing converters that use gapped multiwinding inductors. Therefore, a frequency-dependent model is required that accurately

predicts the magnetic field distribution in the core window and air gap. Previously, this was usually done with FEM simulations or measurements⁽⁵⁾⁽⁸⁾. However, FEM simulations are computationally intensive and therefore not well suited for optimization, which is essential in optimization-based converter design.

A comprehensive list of analytical models that compute the 2D magnetic field in gapped core windows and the resulting winding loss is given in existing literature⁽⁹⁾. However, these models specifically compute the losses only for one type of windings (solid round or foil conductors). Only one model is found in literature, that takes inductors with mixed winding types into account⁽¹⁰⁾. However, this model is iterative and hence, computationally intensive. Furthermore, there is no analytical model predicting the increased eddy current losses and the drop in inductance due to the shielding effect induced by the air gap field.

Hence, this paper proposes an analytical magnetic field model of the core window, from which the frequency dependent self- and mutual impedances of gapped multiwinding inductors are derived. The proposed model considers all relevant physical effects i.e., skin,- proximity,- the fringing effect of the air gap field, and the shielding effect of foil conductors. Moreover, the paper presents an impedance matrix based equivalent circuit (IMEC) that exclusively contains the calculated self- and mutual impedances as degrees of freedom. The model is verified with 3D FEM simulations and experimentally. Therefore, this paper provides a novel equivalent circuit representation of multiwinding magnetic devices as well as the necessary comprehensive analytical model to acquire the required circuit elements. Hereby, the analytical modelling of the 2D air gap field for a combination of different conductor types and their respective physical behavior are the main

This paper is based on Reference⁽¹⁾, which is published in the International Power Electronics Conference (IPEC-Himeji 2022-ECCE Asia) ©2022 IEEJ.

a) Correspondence to: ewald@hpe.ee.ethz.ch

* Laboratory for High Power Electronic Systems (HPE)
 ETH Zuerich, Physikstrasse 3, CH-8092, Switzerland

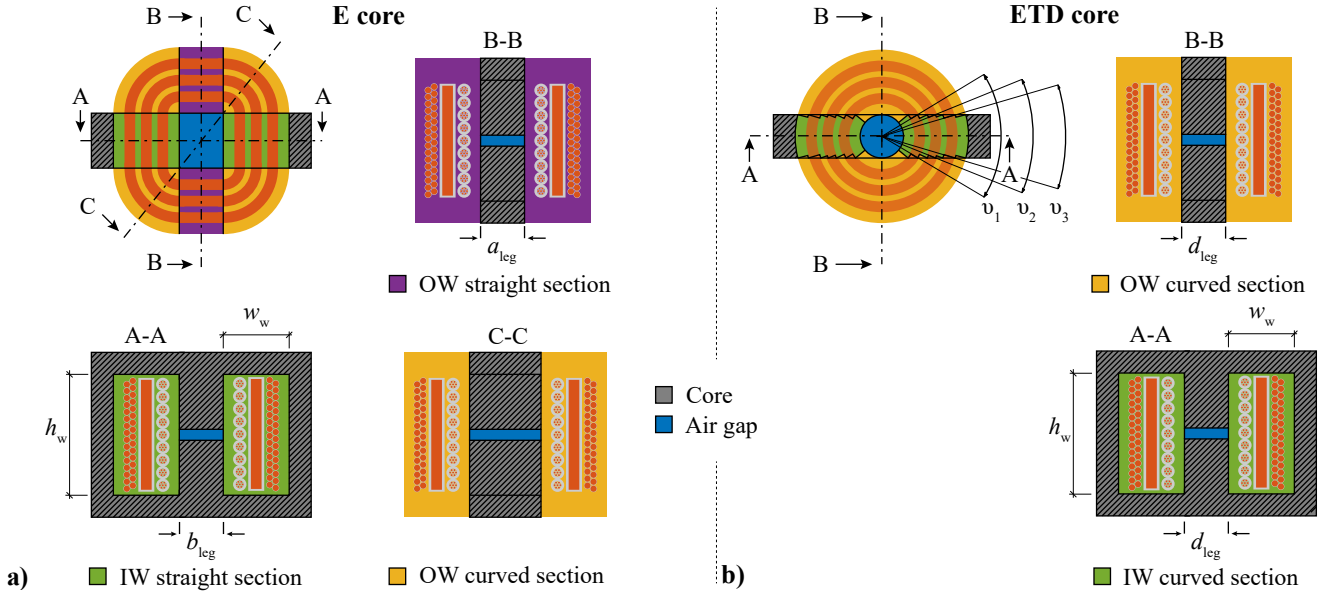


Figure 1 Assumed geometry of a gapped multiwinding inductor. **a)** Inside-window (IW) and outside-window (OW) cross-section, and straight and curved sections of an E core inductor. **b)** IW and OW cross-section for an ETD core inductor, with only curved sections, but different angles for each layer.

focus of the modelling.

The paper is organized as follows: Section 2 defines the geometry of the gapped multiwinding inductor. In sec. 3, the frequency-dependent self- and mutual impedances of multiwinding magnetic devices are derived via the dissipated losses and the stored magnetic energy and the IMEC is presented. The losses and the magnetic energy are derived analytically in sec. 4, and sec. 5 presents the analytical expressions of magnetic field and current density. Finally, sec. 6 verifies the proposed model. Additional notes on computation times and the measurements are provided.

The paper is condensed for space reasons, all important equations are given in the paper, together with the necessary explanations. More specific formulas are provided by the references.

2. Geometry of Gapped Multiwinding Inductor

Gapped multiwinding inductors consist of a gapped core with an arbitrary number of windings. This paper assumes a geometry, in which all windings are wound around the center leg. The resulting geometry is modelled based on two elementary cross-sections: The inside-window (IW) and the outside-window (OW), cf. Fig. 1. Depending on the core type, the inductor consists of different winding sections that are highlighted with different background colors in Fig. 1. Fig. 1a shows the winding section composition of an inductor with E-core whereas Fig. 1b shows an inductor with ETD-core.

Each considered 2D cross-section is divided into several rectangular layers representing non-conductive layers (N-layers), foil conductors (F-layers), and layers of solid round (SR) or Litz wire (L) conductors that are transformed to an equivalent foil conductor (E-layers) as indicated in Fig. 2. The individual currents in each layer and the widths of the respective layers are introduced as variables so that the resulting model is able to describe the magnetic field of multiwinding

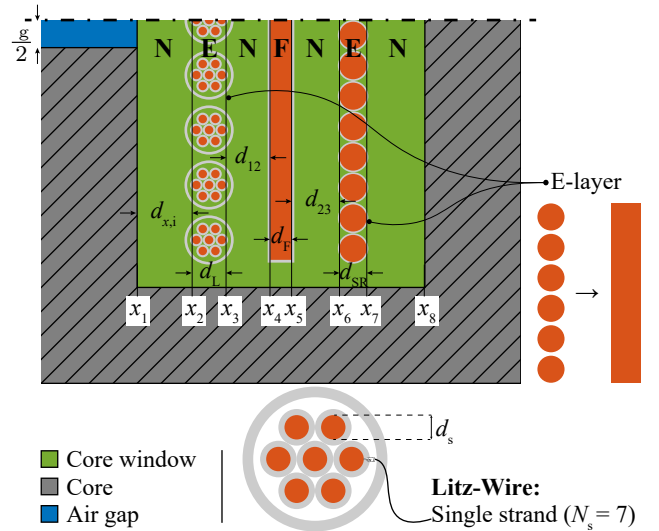


Figure 2 Geometrical definition of layers. Solid round and Litz wire layers are transformed to an equivalent foil conductor (E-layer), where (15) must be satisfied. Foil conductors are referred to as F-layers. All layers in between the windings that do not conduct a current are referred to as N-layers. Furthermore, the definition of Litz wire is given, where N_s is the number strands, and their respective strand diameter is d_s .

devices in different operating modes (currents with different amplitudes and phase angles). This modelling approach is a combination of the models presented in⁽⁷⁾⁽¹¹⁾, where the individual models for F-⁽⁷⁾ and E-layers⁽¹¹⁾ are introduced and utilized to analytically calculate the winding losses and inductance of a single winding inductor.

With the combination of the aforementioned models, this paper proposes a novel analytical model for the computation of the 2D magnetic field in the core window, considering all types of conductors and the physical behavior of each type, respectively (skin, proximity, and shielding effect).

3. Impedance Matrix Equivalent Circuit of Multiwinding Magnetic Devices

The electrical terminal behavior of a multiwinding magnetic device is fully represented by its impedance matrix $\underline{\mathbf{Z}} \in \mathbb{C}^{K \times K}$, where K is the number of windings of the magnetic device. The impedance matrix $\underline{\mathbf{Z}}$ is a symmetrical square matrix that holds the self impedances \underline{Z}_{ii} of each winding and the mutual impedances $\underline{Z}_{ij} = \underline{Z}_{ji}$ between the different windings⁽¹²⁾⁽¹³⁾. Both, self- and mutual impedances are directly measurable parameters of the K -winding magnetic device.

The impedance matrix $\underline{\mathbf{Z}}$ can be derived from the complex power \underline{S} according to (1),

$$\underline{S} = 1/2 \underline{\mathbf{I}}^\dagger \underline{\mathbf{Z}} \underline{\mathbf{I}} \dots \dots \dots (1)$$

where $\underline{\mathbf{I}}$ is the vector of the winding currents and $\underline{\mathbf{I}}^\dagger$ denotes the hermitian of $\underline{\mathbf{I}}$. Since capacitive effects are neglected in this paper, the impedance matrix $\underline{\mathbf{Z}}$ and the complex power \underline{S} can be computed according to (2) and (3)

$$\underline{\mathbf{Z}} = \mathbf{R} + j\omega \mathbf{L} \dots \dots \dots (2)$$

$$\underline{S} = P + j\omega W \dots \dots \dots (3)$$

with the equivalent series resistance matrix \mathbf{R} , the equivalent series inductance matrix \mathbf{L} , the power losses P and the stored magnetic energy W . Note that models of the complex power will be presented in section 4.

To calculate the impedance matrix of a K -winding device, two cases are considered that simplify the impedance matrix calculation⁽¹⁴⁾, (cf. sec. 5):

Case A The i -th winding current is non-zero $I_i \neq 0$ and all the other winding currents are zero.

Case B Two winding currents I_i and I_j are non-zero, all other winding currents are zero. The MMF is assumed to be balanced, i.e., $N_i I_i = -N_j I_j$ is assumed, where N_i and N_j are the number of turns of winding i and winding j , respectively.

With these two cases all self- and mutual impedance can be calculated according to (4) and (5)

$$\underline{Z}_{ii} = \frac{2\underline{S}}{|I_i|^2} \dots \dots \dots (4)$$

$$\underline{Z}_{ij} = \frac{\underline{S} - ((\underline{Z}_{ii}|I_i|^2)/2 + (\underline{Z}_{jj}|I_j|^2)/2)}{|I_i||I_j| \cos(\phi_{ij})} \dots \dots \dots (5)$$

where ϕ_{ij} is the phase angle difference between the winding currents I_i and I_j . Note, that $N_i I_i = -N_j I_j$ implies $\cos(\phi_{ij}) = -1$. Also note, that the current I_i is the current through winding i , hence $N_{1,n} I_i$ is the total current that flows through the layer n of winding i in the 2D plane where $N_{1,n}$ represents the number of turns of layer n . This is especially relevant for E-layers (Litz and solid round wire), whereas F-layers (foils) are assumed to consist of a single turn, i.e. $N_{1,n}^{(F)} = 1$. Vertically stacking multiple foils into one layer is not considered in this paper.

The impedance matrix of a K -winding magnetic device can be graphically represented by a K -port necessary-and-sufficient equivalent circuit (n&s-EC), in which each winding

is represented by a port⁽⁸⁾⁽¹³⁾. Such n&s-EC are characterized by having exactly the number of parameters that can be extracted by independent measurements from the magnetic device. K -port n&s-EC as well as the impedance matrix $\underline{\mathbf{Z}}$ are uniquely defined by $K(K+1)/2$ parameters⁽¹³⁾⁽¹⁵⁾. EC are useful as they enable the implementation of K -winding devices in circuit simulations and facilitate their implementation in converter optimizations.

Fig. 3 proposes the impedance matrix equivalent circuit (IMEC) that exclusively consists of self- and mutual impedances. It uses $K(K-1)/2$ sub-circuits to represent the mutual impedances. These sub-circuits are based on the conventional 2-winding T-EC⁽¹⁶⁾ shown in Fig. 3a and each sub-circuit satisfies (6).

$$\begin{bmatrix} \underline{V}_i \\ \underline{V}_j \end{bmatrix} = \begin{bmatrix} 0 & \underline{Z}_{ij} \\ \underline{Z}_{ij} & 0 \end{bmatrix} \begin{bmatrix} \underline{I}_i \\ \underline{I}_j \end{bmatrix} \dots \dots \dots (6)$$

The proposed IMEC is a fully determined physical representation of the multiwinding magnetic device with the advantage of exclusively containing measurable parameters. The IMEC can also be adapted such that it contains ideal transformers with turn ratios that represent the turn ratios of the windings on the magnetic device. Furthermore, the number of circuit elements can be reduced by introducing a leakage impedance (7). The result of the aforementioned variations lead to the adapted IMEC shown in Fig. 4.

$$\underline{Z}_{\sigma,i} = \underline{Z}_{ii} - \sum_{\substack{j=1 \\ j \neq i}}^K \frac{N_i}{N_j} \underline{Z}_{ij} \dots \dots \dots (7)$$

As shown in⁽¹⁾, the self- and mutual impedance can also be used to derive the elements of other EC such as the Extended Cantilever Model (ECM) presented in⁽¹⁵⁾. Although both representations are equivalent, the IMEC is advantageous for several reasons. First, the ECM is based on the admittance matrix, which requires inverting the impedance matrix. Second, some elements of the ECM are difficult to measure, since they require measuring currents in short-circuited windings, making the ECM difficult to verify directly.

With the IMEC, this paper proposes a novel equivalent circuit representation of a multiwinding magnetic devices, which is very compact by introducing T-elements (cf. Fig. 3), but on the other hand considers resistive and reactive components, and therefore the impedance of the device. The IMEC can be used in circuit simulations very easily.

4. Computation of the complex power

As discussed in sec. 3, the self impedances \underline{Z}_{ii} are computed via the complex power \underline{S} which is obtained from the magnetic energy and the dissipated power according to (8)

$$\underline{S} = \left(\sum_{n=1}^N \lambda_n P'_n + \vartheta_n P''_n \right) + j\omega \left(W_c + \sum_{n=1}^N \lambda_n W'_n + \vartheta_n W''_n \right) (8)$$

where λ_n is the total length of all straight sections of the n -th layer and ϑ_n is the total angle of all circular sections of the n -th layer[†].

[†] Note that n refers to all geometrically defined layers, hence, also non-conductive layers. Whereas the power losses in the non-conductive layers is zero, the magnetic energy is non-zero.

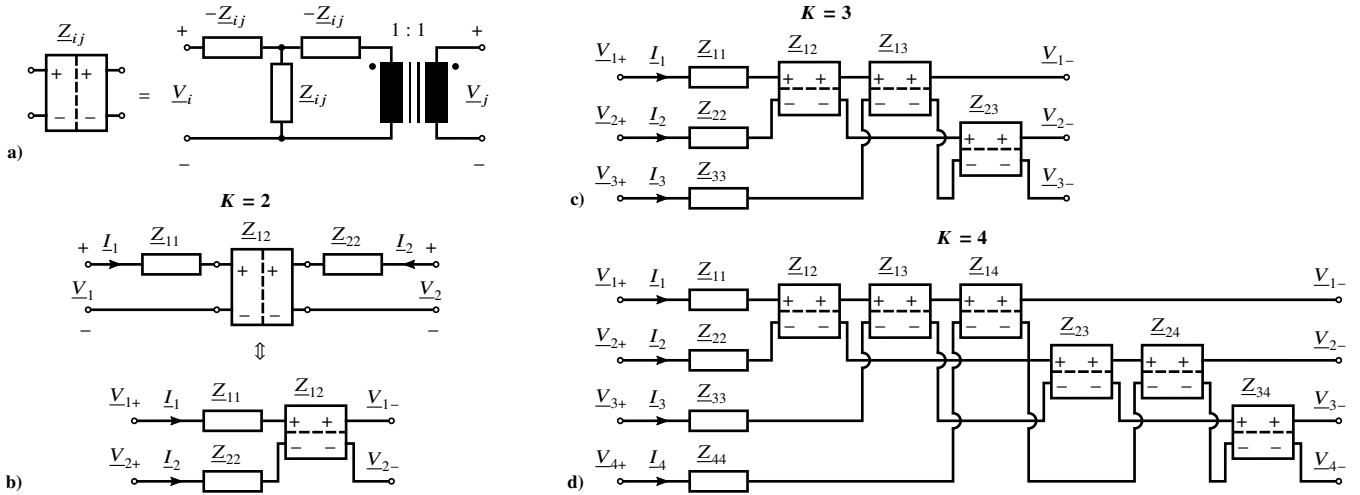


Figure 3 Impedance Matrix based equivalent circuit (IMEC) representation of K -winding magnetic device that exclusively contains self- and mutual impedances. **a)** T-element EC, **b)** IMEC of a 2-winding magnetic device, **c)** IMEC of a 3-winding magnetic device, **d)** IMEC of a 4-winding magnetic device.

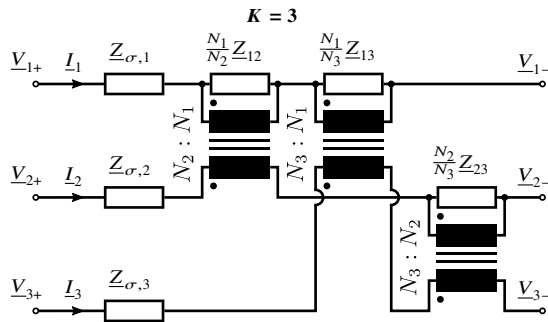


Figure 4 Adapted version of the IMEC from Fig. 3 that requires fewer circuit elements and contains the turn ratios of the multiwinding magnetic device.

In contrast to the self impedances, the mutual impedances Z_{ij} are treated as follows. The complex power is computed in two steps, where the real part of the mutual impedance is obtained using the models from sec. 4.2 and the real part of (8). The imaginary part (energy of the leakage field) is obtained using the Double-2D modelling approach presented in⁽¹⁷⁾. Here, the IW and OW energy contribution are acquired by calculating the energy per unit length multiplying each with an energy weighted length (partial leakage length)⁽¹⁷⁾. Further details can be found in section 5.2.

The following subsections briefly explain the calculation of the magnetic energy per unit length (p.u.l.) W'_n & magnetic energy per unit angle (p.u.a.) W''_n , the power losses p.u.l. P'_n & p.u.a. P''_n , and the stored magnetic energy in the core W_c .

4.1 Magnetic energy calculation The magnetic energy is linked to the reactive part of the impedance. For straight winding sections, the magnetic energy p.u.l. W' is computed with (9)[†]

$$W' = \frac{\mu_0}{2} \iint_{\mathcal{A}} \vec{H} \cdot \vec{H}^* dA \dots \dots \dots (9)$$

and scaled linearly with the length of the individual section

[†] Note that all complex fields in this paper denote the phasor of the particular field quantity.

(cf. sec. 2). For curved winding sections, (10)

$$W'' = \frac{\mu_0}{2} \iint_{\mathcal{A}} x \vec{H} \cdot \vec{H}^* dA \dots \dots \dots (10)$$

yields the magnetic energy p.u.a. which is scaled with the angle of the corresponding curved winding section. With (9) and (10), the total magnetic energy stored in IW and OW winding sections is obtained.

In addition, the magnetic energy that is stored in the core and in the air gaps^{††} (11)

$$W_c = \frac{\mu_0}{2} |\underline{H}_g|^2 \left(N_g V_g + \frac{V_e}{\mu_r} \right) \dots \dots \dots (11)$$

where V_g is the volume of a single air gap, N_g is the number of air gaps in the center leg, \underline{H}_g is the spatially homogeneous magnetic field in the air gap (21), and μ_r is the relative permeability of the core material. For the magnetic energy in the core, it is assumed that $\underline{B}_c = \mu_0 \underline{H}_g$, which neglects any fringing paths. Furthermore, V_e is the effective volume of the core and is typically given by the manufacturer's data sheet. The magnetic field models used for calculating the fields \vec{H} and \underline{H}_g introduced above are derived in (20) and (21).

4.2 Power losses calculation The resistive part of the impedance is computed with the power losses per unit length:

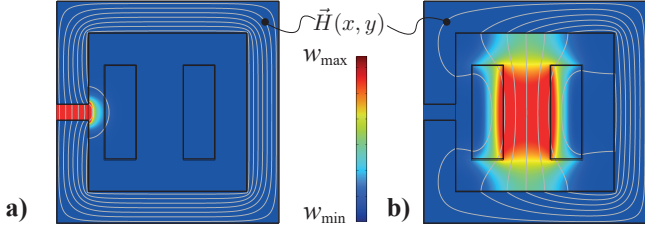
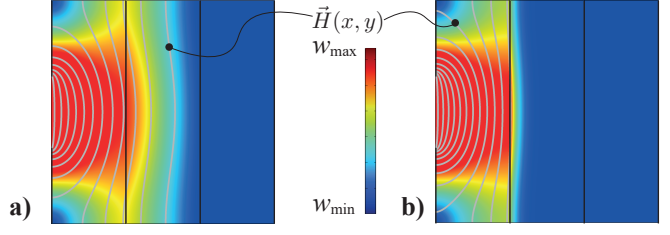
$$P' = \frac{1}{2\sigma} \iint_{\mathcal{A}} \vec{J} \cdot \vec{J}^* dA \dots \dots \dots (12)$$

whereas the power losses per unit angle is

$$P'' = \frac{1}{2\sigma} \iint_{\mathcal{A}} x \vec{J} \cdot \vec{J}^* dA \dots \dots \dots (13)$$

where (12) and (13) are used for F-layers. The integration must be evaluated for every F-layer in the core window. The current density is analytically derived from the magnetic potential as (22) in sec. 5. The integrals (12) and (13) are solved

^{††} The fringing paths of the air gap field are neglected in the calculation of stored magnetic energy. Nevertheless, the fringing paths are considered in the magnetic field formulas for the core window.


 Figure 5 a) $I_1 \neq 0 \wedge I_2 = 0$ b) $I_1 = -I_2$

 Figure 6 a) $f = 10 \text{ Hz}$. b) $f = 100 \text{ kHz}$.

analytically as well⁽⁷⁾⁽⁹⁾.

In E-layers, the integration of the inhomogeneous current density distribution inside the boundaries of a cylindrical conductor is already performed in polar coordinates⁽¹¹⁾. This leads to an analytical expression of the power losses of the respective conductor depending on the net current, the frequency, and an assumed homogeneous external magnetic field. The latter is replaced by the squared averaged magnetic field over the considered volume of an E-layer⁽¹¹⁾.

In particular, the squared averaged magnetic fields, p.u.l. and p.u.a., are obtained by averaging the magnetic field over either straight or curved winding sections, respectively. Eventually, this leads to closed-form analytical expressions of the power losses P' (p.u.l.) and P'' (p.u.a.) of the individual conductors in an E-layer, and finally, to the overall losses dissipated in the E-layer. As done in⁽¹¹⁾, the resulting expressions are adapted to Litz wire if required.

The height of each layer is either assumed to equal the physical layer height (cf.⁽⁷⁾) or the core window height h_w (cf.⁽¹¹⁾), depending on the model that is used to model the magnetic field of the respective layer.

5. Mathematical models of the 2D magnetic field

This section presents the models of the magnetic field in the core window and in the air gaps that are combined according to the flowchart in Fig. 7. As elaborated in sec. 4, the resistive and the reactive part of the impedance (2) both depend on the magnetic field. The different entries of the impedance matrix are calculated using different cases of the excitation of the windings as discussed in sec. 3. Depending on these cases, the magnetic field has significantly different distributions to be taken into account when calculating the magnetic field analytically. Two cases and their resulting field distributions are distinguished (cf. sec. 3):

Case A Only one winding current is non-zero and the other windings are open-circuited resulting in a non-zero total magneto motive force (MMF $\neq 0$). In this case, the magnetic energy is predominantly stored in the air gap as the main field path leads through the core as shown in Fig. 5a. The magnetic field in the air gap causes a fringing field around the air gap which affects windings in close proximity and decreases the reluctance of the core.

Case B The total MMF is zero, i.e. $\sum_i N_i I_i = 0$, which is achieved by setting $N_i I_i = -N_j I_j$ and every other current to zero in this paper. This condition cancels the coupling flux between the windings completely, i.e. the field lines lead through the air between the windings (leakage field, cf. Fig. 5). Hence, the

magnetic energy is stored mainly between the windings and the air gap contains almost no energy. FEM simulations have shown that the energy stored in the core window exceeds the air gap energy by about five orders of magnitude. Therefore, the analytical models neglect the air gap in this configuration.

5.1 Model for non-zero total MMF As stated before, the majority of the magnetic energy is stored in the air gap if the total MMF is non-zero. Hence, the air gap magnetic energy is predominant compared to the window energy and therefore only the IW cross-section (cf. Fig. 1a) is considered. The air gap fringing field has a significant influence on the magnetic field and the derived impedance, especially if foil conductors are in the vicinity of the air gap as they shield the fringing field with increasing frequency⁽⁷⁾. Fig. 6 shows the air gap field with a foil in close proximity to the air gap. At low frequencies, the air gap field penetrates through the foil (Fig. 6a). At higher frequencies, the air gap field induces significant eddy currents within the foil which counteract the magnetic air gap field and therefore shield the magnetic air gap field as shown in Fig. 6b).

For the purpose of taking this effect into account, a novel model is proposed that divides the core window into separate regions as shown in sec. 2. For each region, a magnetic vector potential formulation satisfying the governing partial differential equation of the respective region (written in superscript), is proposed. The governing equations are:

$$\underline{\Delta}_z^{(N)} = 0 \dots\dots\dots (14)$$

$$\underline{\Delta}_z^{(E)} = -\mu_0 \underline{J}_n^{(E)} \dots\dots\dots (15)$$

$$\underline{\Delta}_z^{(F)} = \underline{\gamma}^2 \underline{A}_z^{(F)} \dots\dots\dots (16)$$

Here, $\underline{J}_n^{(E)} = N_{i,n} I_i / A_{\text{layer}}$ is the spatially homogeneous current density in the E-layer, I_i is the current (amplitude) through the windings of the E-layer (cf. sec. 2), $\underline{\gamma} = (1+j)/\delta$, and δ is the skin depth. The magnetic vector potentials only have a z -component as the current is only through-plane, and are given as

$$\begin{aligned} \underline{A}_z^{(N)} &= \underline{B}_0(x-x_n) \\ &+ \sum_{k=1}^{\infty} (\underline{C}_k e^{-p_k(x-x_n)} + \underline{D}_k e^{p_k(x-x_n)}) \cos(p_k y) \end{aligned} \quad (17)$$

$$\begin{aligned} \underline{A}_z^{(E)} &= \underline{B}_0(x-x_n) + \underline{C}_0(x-x_n)^2 \\ &+ \sum_{k=1}^{\infty} (\underline{C}_k e^{-p_k(x-x_n)} + \underline{D}_k e^{p_k(x-x_n)}) \cos(p_k y) \end{aligned} \quad (18)$$

$$\underline{A}_z^{(F)} = \underline{M}_0 e^{-\underline{\gamma}(x-x_n)} + \underline{N}_0 e^{\underline{\gamma}(x-x_n)}$$

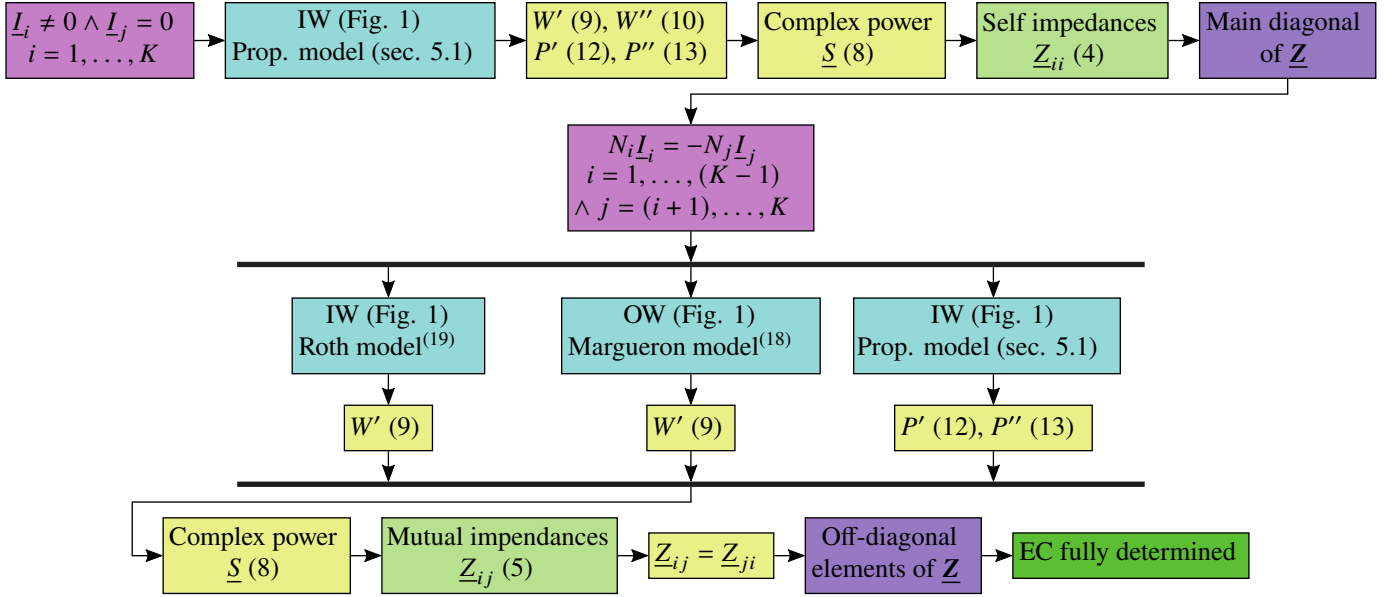


Figure 7 Overview of the proposed modelling process. See sections 3 – 5 and the given references for details.

$$+ \sum_{k=1}^{\infty} \left(\underline{M}_k e^{-\xi_k(x-x_n)} + \underline{N}_k e^{\xi_k(x-x_n)} \right) \cos(p_k y) \quad (19)$$

where x_n references the x -origin of the n -th layer, as defined in Fig. 2. The coefficients in the equations above are determined with boundary conditions at the window edges and with interface boundary conditions between the different layers, which leads to a system of linear equations⁽⁷⁾⁽⁹⁾⁽²⁰⁾. In addition, (18) is given to satisfy (15) in E-layers, where the magnetic field distribution is assumed to be independent of the frequency⁽¹¹⁾. The analytical magnetic field expressions considering the air gap fringing field are obtained from (20).

$$\vec{e}_x \underline{H}_x + \vec{e}_y \underline{H}_y = 1/\mu_0 \vec{\nabla} \times \left(\vec{e}_z \underline{A}_z \right) \dots \dots \dots \quad (20)$$

Hence, the magnetic field \vec{H} has components in x - and y -directions. The coefficients \underline{B}_0 , \underline{M}_0 , and \underline{N}_0 depend on the currents in the individual windings. The coefficients \underline{C}_k , \underline{D}_k , \underline{M}_k , \underline{N}_k , ξ_k and p_k define the air gap fringing field, where the tangential components of the magnetic field on all surfaces of the core window are used to solve the boundary value problem. Hereby, the magnetic field is zero along every surface, except in the air gap, where it has the constant value:

$$\underline{H}_g = \frac{k_\mu}{N_g l_g} \sum_i N_i I_i, \quad k_\mu = \frac{1}{1 + l_e / (\mu_r N_g l_g)} \dots \dots \quad (21)$$

Here, l_g is the air gap height, N_g is the number of gaps (all placed periodically in the center leg, with symmetry to the x -axis), and l_e is the effective path length of the core, typically given by the manufacturer. Furthermore, μ_r is the relative permeability of the core. The missing coefficient \underline{C}_0 of the additional E-layer field (18) is obtained by substituting (18) into (15).

The inhomogeneous current density inside F-layers is directly obtained from the magnetic potential:

$$\underline{J}_z^{(F)} = -\gamma^2 / \mu_0 \underline{A}_z^{(F)} \dots \dots \dots \quad (22)$$

Note that the proposed winding layer model in this section

Table 1 Submodels used for calculating the imaginary part of (8) in Case B (balanced magneto motive forces, MMF = 0).

W'_{IW}	Roth	(19)
W'_{OW}	Margueron 2010	(18)
$l_{p,IW}$	Empirically Corrected Axial Flux (ECAFF)*	(17)
$l_{p,OW}$	Empirically Corrected Axial Flux (ECAFF)*	(17)

*Axial Flux model, if ECAFF not applicable to or not valid for particular geometry

assumes the layer heights to be equal to the window height h_w (cf. Fig. 1). The proposed model is a combination of the models presented in⁽⁷⁾⁽¹¹⁾ which are based on the works⁽⁹⁾⁽²⁰⁾.

The novelty of the proposed model is in its ability to consider all relevant conductor types in one core window, and take into account the respective physical behavior in terms of the relevant loss mechanisms (skin, proximity, and shielding effect).

5.2 Models for zero total MMF In the case of a total MMF of zero, the main field path leads through the air between the windings (cf. Fig. 5b). Here, two different cross-sections must be considered: The inside window (IW) section and the outside window (OW) section⁽¹⁷⁾ shown in Figs. 1a&b. The reason is that the magnetic field distribution and hence the magnetic energy density are predominantly influenced by the position of the core yokes and the outer leg, rather than the air gap.

Analytical models of the IW and OW energy per unit length W' are chosen based on the comparison executed in⁽²¹⁾. These energies per unit length are multiplied by energy weighted mean lengths (partial leakage lengths l_p) to acquire the total IW and OW energy contributions⁽¹⁷⁾. The submodels used for computing energy per unit length and partial leakage length are listed in Tab. 1.

These models are selected as they perform best with respect to high accuracy and low computational effort⁽²¹⁾.

Table 2 Parameters of prototype and 3D FEM inductors. Cf. Figs. 1 and 2 for geometric parameter definitions. Note that the layer thickness t_1 in Tab. 2 depends on the winding type and denotes the Litz wire (outer) diameter d_L , the SR wire diameter d_{SR} , and the foil thickness d_F (all without insulation), respectively. Q_1 denotes the number of layers of the particular winding. a_i and h_i are the total winding width and the total winding height (all without insulation), respectively. Additionally, the permeability of the material was considered in the analytical modelling using (21), which makes it possible to compare cores with different permeability.

Unit	Core data					Winding 1					Winding 2					Winding 3					Inter wdg.					
	l_g	d_{leg}	h_w	w_w	μ_r	Type	a_1	h_1	N_1	Q_1	t_1	Type	a_2	h_2	N_2	Q_1	t_1	Type	a_3	h_3	N_3	Q_1	t_1	$d_{x,i}$	d_{12}	d_{23}
3D FEM	1	22.1	44	10.75	5000	SR	0.7	39.65	42	1	0.7	Foil	1.8	40	4	4	0.3	SR	0.7	39.65	42	1	0.7	1	0.23	0.23
No.1**	2	22.1	44	10.75	1590	Litz*	1	41	33	1	1	Foil	1.9	40	10	10	0.1	SR	0.8	40.5	28	1	0.8	1.2	0.25	2.25
No.2**	1	12.6	29.1	8.7	1600	SR	2.4	25.6	34	2	0.8	Litz*	2.25	26	42	2	1	-	-	-	-	-	1.5	1.5	-	

*360 insulated strands, strand diameter = 40 μ m.

**Core material: N87, TDK⁽²²⁾.

6. Model Verification

This section verifies the presented models with 3D FEM simulations and measurements. For that purpose, a 3D FEM model and two prototype inductors shown in Figs. 8 & 9, were built. A list of parameters of the FEM model and the inductor prototypes are given in Tab. 2.

There are two main reasons for the two-step verification: First, using (3D) FEM makes it possible to have a benchmark that is comparable in its nature. Both, analytical model and FEM are not prone to manufacturing tolerances, etc.: Both can be set up exactly the same, so that the results should match exactly at best. The reason for using 3D FEM instead of sectionized 2D FEM, as used by the proposed model, is that the 2D OW sections of a correct physical model would generate a different air gap field as the 3D version due to

the available magnetic paths and Ampere's law. This must be circumvented by introducing current densities instead of air gaps on the core surface. A true 3D model is therefore more trustworthy in the context of the generated air gap field. The second reason for the two-step verification is the use of Litz wire. It is nearly impossible to compute a full 3D FEM model containing multiple stranded and twisted wires, as can be concluded from literature on the topic⁽²³⁾.

The 3D FEM simulation is used to confirm the model's accuracy without possible influences from geometric tolerances and the result is shown in Fig. 10a. The computed self- and mutual impedances are split into resistive and reactive parts (R_{ij} & L_{ij}). The results obtained with the proposed model match the simulated results of the 3D FEM very well over a wide frequency range. Note that the curves of the self resistances R_{11} and R_{33} slightly differ from typical curves of round wire's AC resistance from literature⁽¹¹⁾. This deviation is caused by additional eddy current losses that are induced in the (open-circuited) foil winding by the air gap fringing field. These eddy currents also shield the magnetic field from propagating further into the core window and hence cause a drop in the self inductance of all windings. Moreover, at elevated frequencies, the mutual resistances[†] become more significant so that they cannot be neglected in loss calculation anymore. The measurements shown in Fig. 10b&c also prove that the proposed model predict the self- and mutual resistances and inductances of the magnetic device accurately. In the following, the most noteworthy measurement results and physical effects are discussed based on individual plots, instead of those shown in Fig. 10, for the sake of visibility.

Fig. 11 shows the self resistance of the Litz wire winding of prototype No.1. Here, the self resistance of the Litz wire winding is heavily dominated by the air gap fringing field induced eddy current losses in the foil. As a reference, the expected resistance increase of the same Litz wire winding without additional windings in the core window⁽¹¹⁾ are also shown in Fig. 11 (w/o other windings). Without other windings present, the Litz wire winding resistance starts to increase at much higher frequencies due to its very thin strands, as expected. Hence, the presence and the positioning of additional windings in multiwinding devices, as for example when using foils⁽³⁾⁽⁵⁾, is crucial for the overall losses of the component. The newly proposed model in this paper allows for taking

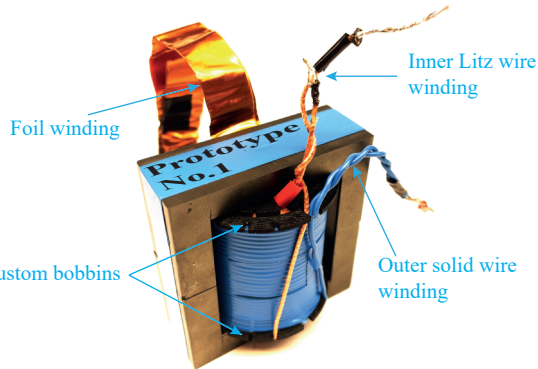


Figure 8 Inductor prototype No.1 with 3 windings: Litz wire (inner), foils (middle), and solid wire (outer).

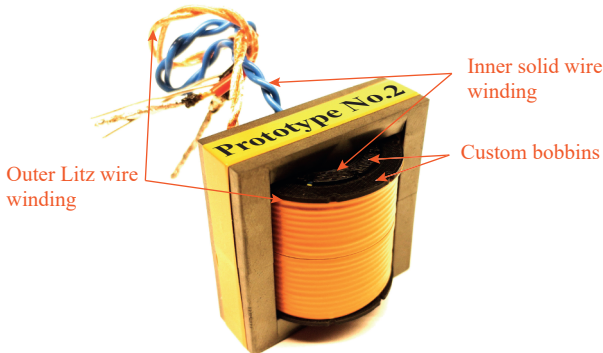


Figure 9 Inductor prototype No.2 with 2 windings: Solid wire (inner) and Litz wire (outer).

[†] Mutual resistances refer to the additional power losses in multiwinding devices if two windings are excited at the same time⁽²⁴⁾

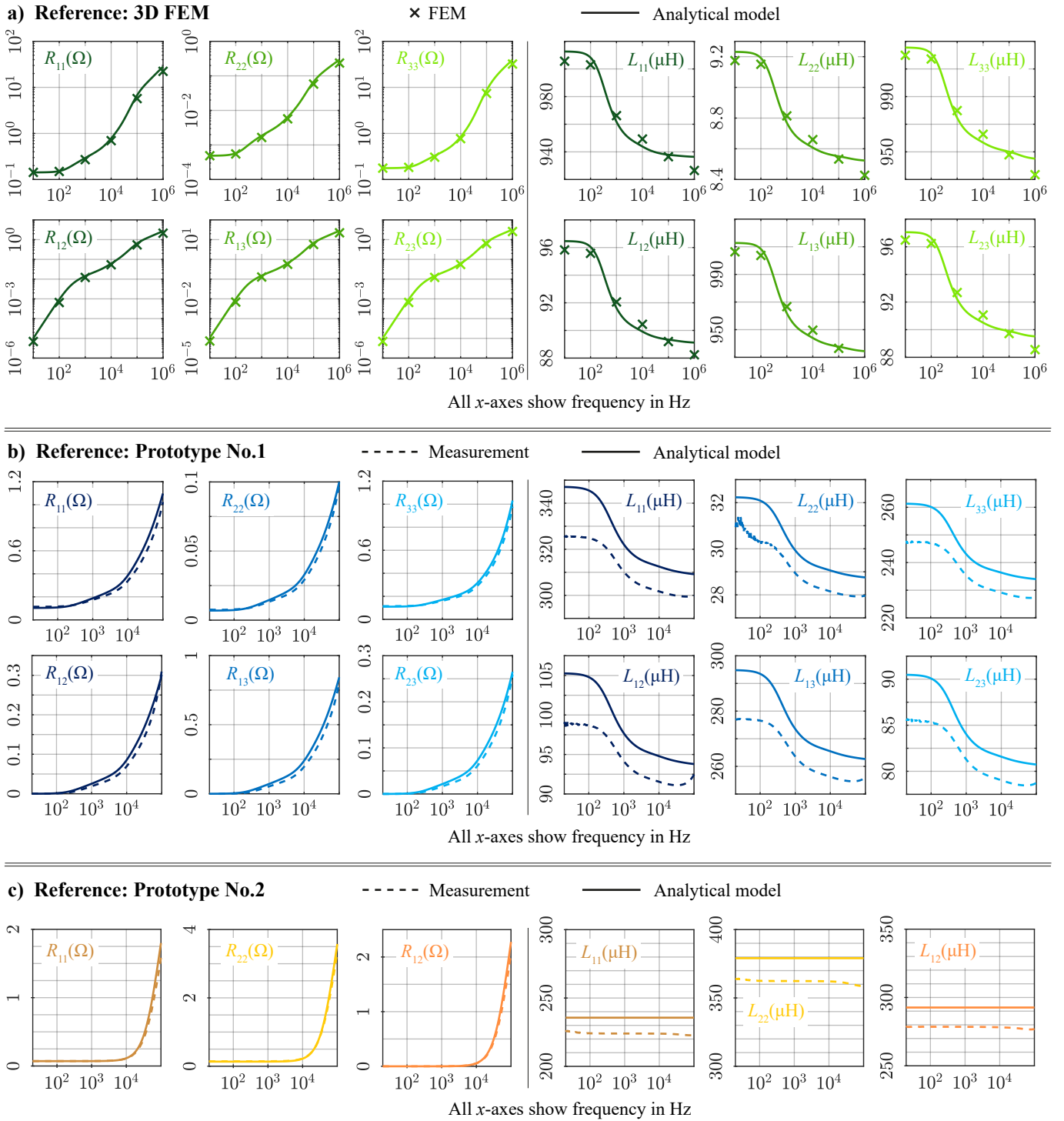


Figure 10 Comparison of the results obtained with the proposed model with **a)** 3D FEM, **b)** 3-winding inductor prototype, and **c)** 2-winding inductor prototype. Note, that the inductances L_{11} and L_{33} in **a)** are slightly different, even though they have the same number of turns. The reason is that the outer winding 3 has a larger winding diameter than the inner winding 1 and hence, more energy is stored in the space between the winding and the center leg leading to a slightly larger inductance L_{33} .

these effects into account accurately.

Since prototype No.1 holds windings of different winding types, it is difficult to distinguish between induced eddy current losses in the foil and in any SR winding close to the air gap which both affect the effective resistance of the Litz wire. To examine this more closely, inductor prototype No.2 is designed without foil windings. Instead, SR windings are used

for the winding in proximity to the air gap (cf. Tab. 2). The results shown in Fig. 12 prove that Litz wire windings, or more general windings with small diameter, are always affected by those with a larger diameter. Again, the expected effective resistance increase $F_{R,22}$ without the additional SR winding is plotted as a reference (cf. Fig. 12, w/o SR winding).

The self inductance L_{11} of prototype No.1 vs. frequency is

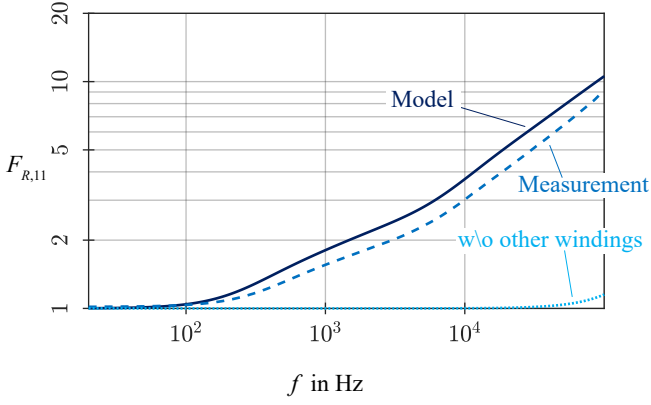


Figure 11 Relative resistance increase $F_{R,11}=R_{11}(f)/R_{11}(0)$ of the primary winding (Litz) of inductor prototype No.1. The results show that the effective resistance of the Litz wire winding increases significantly due to the air gap fringing field induced eddy currents in the foil.

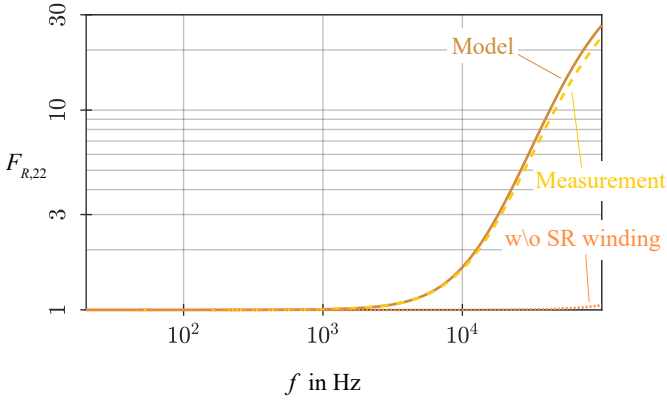


Figure 12 Relative resistance increase $F_{R,22}=R_{22}(f)/R_{22}(0)$ of the secondary winding (Litz) of inductor prototype No.2. The additional plot of the expected resistance increase of the Litz wire winding without the solid round wire winding shows, that the majority of the winding losses is caused by the open-circuited solid round wire winding in proximity to the air gap.

Table 3 Average relative errors of proposed analytical model in percent

Inductor	L_{11}	L_{22}	L_{33}	L_{12}	L_{13}	L_{23}
3D FEM	0.58	0.59	0.59	0.56	0.53	0.57
Prototype No.1	4.52	3.86	3.89	4.35	4.41	3.99
Prototype No.2	5.18	4.70	-	5.20	-	-

examined more closely in Fig. 13. Here, the self inductance is computed with the manufacturer's A_L value as a reference. The figure shows that the self inductance computed with the A_L -value coincides well with the target value for the DC case. However, at elevated frequencies, the real inductance value tends to be less than the one predicted with the A_L -value. The drop of inductances is caused by the shielding of the foils which affects the self- and the mutual inductances of every winding, as shown in Fig. 10. Overall, the proposed model is able to compute the inductance vs. frequency very accurately. The average error over the full frequency range of the individual inductances is given in Tab. 3 for the 3D FEM and both inductor prototypes based on the measured values. All in all, the proposed analytical model is in the same accuracy range

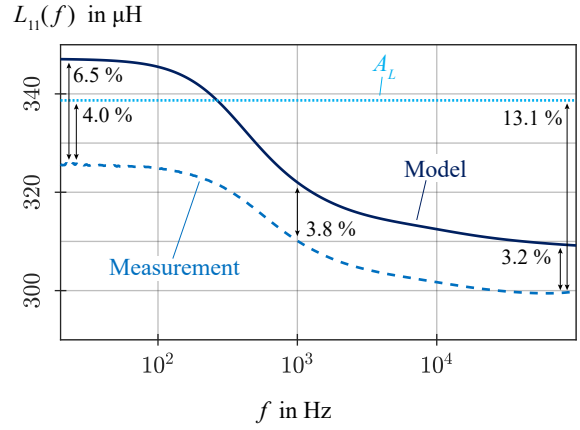


Figure 13 Frequency dependent self inductance $L_{11}(f)$ of the primary winding of inductor prototype No.1. The self inductance decreases due to the shielding effect of the foil conductors⁽⁷⁾. The manufacturer's A_L value does not consider the frequency dependence. Note, that the primary winding of inductor prototype No.1 is no foil winding itself.

as 3D FEM simulations. The increased error in comparison with the measurements are caused by manufacturing tolerances and additional side effects that can neither be modelled analytically, nor with FEM.

Finally, the influence of the air gap fringing field is visualized in Fig. 14. The figure shows the result of a 2D FEM simulation, in which a foil is placed between the air gap and a solid round wire winding. The frequency and the current excitations are varied according to the table in Fig. 14. The

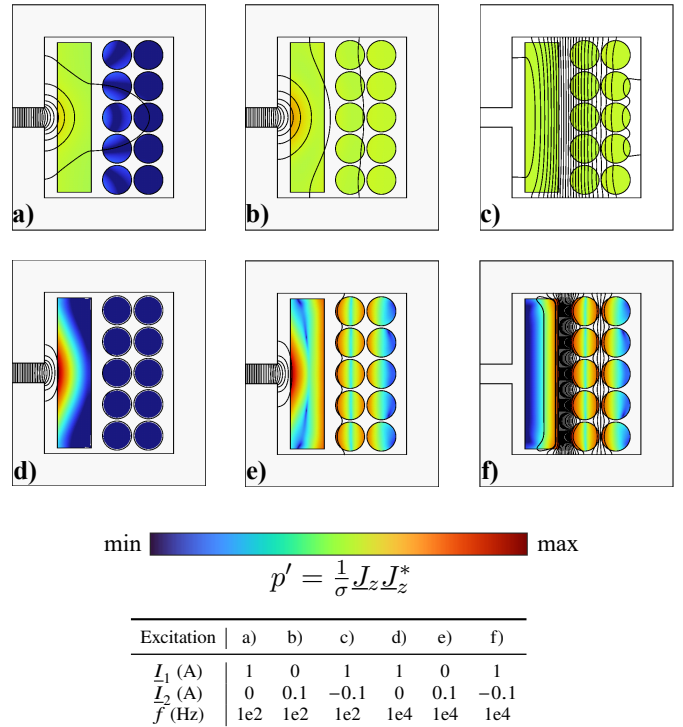


Figure 14 Fringing field effect of the air gap. The magnetic field \vec{H} is indicated by the black field lines, the dissipated power density per unit length $p' = 1/\sigma \underline{J}_z \underline{J}_z^*$ by the colored surface.

plots show that even if the foil conductor is open-circuited, eddy current losses are induced by the air gap's fringing field in the foil. These additional losses occurring in the foil are attributed to the self resistance of the excited winding. This is in accordance with the measurements and the analytically computed results. In contrast to our proposed model, existing models in literature are not capable of correctly taking this effect into account.

In summary, the results in Figs. 10, 11, and 12 show that the self and the mutual resistances can be predicted accurately with the proposed model. In addition, the reactive part (inductance) vs. frequency is in accordance with the measurement (cf. Figs. 10 & 13). Given the fact that almost all inductances are frequency-dependent it is still beneficial to consider the use of the proposed model in contrast to the manufacturer's A_L value, since the proposed model accurately describe the frequency dependence of the inductance. Furthermore, a relative error of less than 5 % over the complete frequency range can still be considered as quite accurate given that geometric tolerance can affect the result in similar orders of magnitude. It becomes apparent that the model accurately predicts the impact of foil conductors in a mixed multiwinding magnetic device⁽²⁾, taking into account the shielding effect of the foils, which makes the model useful in virtual prototyping an optimization of such devices.

6.1 Additional notes on computation times This section provides a quantitative analysis of the computational efficiency of the proposed model. Tab. 4 gives all relevant parameters, as well as the execution times of a single execution and the total execution time of each, a full 3D FEM simulation, a comparable 2D FEM simulation with appropriate meshing[†], and the proposed model, for a two-winding magnetic device (e.g., prototype 2). Note that all computation times are given for a single frequency. Scaling of the computational effort for a device with more than two windings works linearly.

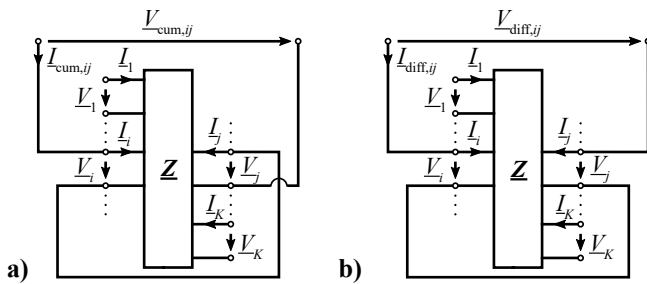


Figure 15 Definition of the cumulative and differential measurements at an K -port network.

6.2 Additional notes on the measurements All measurements were performed with the Keysight E4990A impedance analyzer. Thereby, the self impedances were measured directly, with the other windings open-circuited. The mutual impedances were measured with cumulative and differential measurements⁽²⁵⁾ which are defined in Fig. 15 and (23).

[†] No 2D FEM simulation was used for verifying the model.

$$\begin{aligned} Z_{\text{cum},ij} &= \frac{V_{\text{cum},ij}}{I_{\text{cum},ij}} = Z_{ii} + 2Z_{ij} + Z_{jj} \\ Z_{\text{diff},ij} &= \frac{V_{\text{diff},ij}}{I_{\text{diff},ij}} = Z_{ii} - 2Z_{ij} + Z_{jj} \dots \dots \dots (23) \\ &\Downarrow \\ Z_{ij} &= \frac{Z_{\text{cum},ij} - Z_{\text{diff},ij}}{4} \end{aligned}$$

Note that fundamental energy and power considerations only require \mathbf{R} and \mathbf{L} to be positive (semi-)definite⁽¹³⁾. Thus, $R_{ij} = \Re\{Z_{ij}\} < 0$ and $\omega L_{ij} = \Im\{Z_{ij}\} < 0$ are possible.

7. Conclusion

This paper presents a novel equivalent circuit representation of multiwinding magnetic devices in form of the impedance matrix equivalent circuit (IMEC), and the derivation of its elements from an analytical model of the magnetic field of gapped multiwinding inductors. The model allows for analytically calculating the impedance matrix considering the impact of the skin- & proximity effect and the air gap's fringing field. Thus, a full equivalent circuit (EC) representation in terms of impedances of a gapped multiwinding magnetic device can be computed. The model leads to significantly less computational effort (computations times in the millisecond range) while being in a similar accuracy range as FEM simulations. The novelty of the used analytical model is its capability to consider all relevant conductor types and their respective physical properties in terms of their impact on the magnetic field.

Furthermore, measurements confirm that the impact of the air gap fringing field induced eddy currents in all windings is not negligible. Self- and mutual resistances increase significantly whereas inductances decrease as the eddy currents shield the magnetic field from propagating further into the core window. This paper presents insightful measurements of these phenomena and provides physical explanations, as well as an analytical comprehensive model to describe the effects mathematically.

Acknowledgment

The authors would like to express their acknowledgment to the Baechli AG, Switzerland, and Innosuisse, Switzerland (Appl. No.: 32328.1 IP-ENG), for providing financial support for this project.

References

- (1) T. Ewald, R. Schlesinger, J. P. Agner, and J. Biela, "Frequency-dependent equivalent circuit parameter calculation of gapped multiwinding inductors," in *International Power Electronics Conference (IPEC-Himeji 2022- ECCE Asia)*, 2022, pp. 2425–2432.
- (2) D. Leuenberger and J. Biela, "Accurate and Computationally Efficient Modeling of Flyback Transformer Parasitics and their Influence on Converter Losses," in *EPE, ECCE Europe*, Geneva, 2015.
- (3) R. Yu, G. K. Y. Ho, B. M. H. Pong, B. W. K. Ling, and J. Lam, "Computer-aided design and optimization of high-efficiency LLC series resonant converter," *IEEE Trans. on Power Electronics*, vol. 27, no. 7, pp. 3243–3256, 2012.
- (4) Y.-C. Liu, C. Chen, K.-D. Chen, Y.-L. Syu, and M.-C. Tsai, "High-Frequency LLC Resonant Converter with GaN Devices and Integrated Magnetics," *Energies*, vol. 12, no. 9, 2019.
- (5) J. Zhang, W. G. Hurley, and W. H. Wolfe, "Gapped transformer design

Table 4 Quantitative analysis of computation times of 3D FEM, 2D FEM and the proposed model

Calculation method	2D FEM	3D FEM	Proposed model
Computer	Server Intel® Xeon® Processor E5-2697A v4 @ 2.60 GHz, 16 physical cores	Server Intel® Xeon® Processor E5-2697A v4 @ 2.60 GHz, 16 physical cores	Laptop Intel® Core™ i7-8665U Processor, 4 physical cores
Cores used for computation	16	16	1
Single calculation time*	~25 s	~2400 s	<0.005 s**
Necessary model calculations	9 for E core, 6 for ETD core	3 full model simulations	9 for E core, 6 for ETD core
Total calculation time	~225 s for E core, ~150 s for ETD core	~7200 s	~0.025 s***

*Single model execution. Note, that for the impedance matrix, the 2D FEM and the proposed model must be evaluated more than once.

**Quantitative analysis from literature⁽⁹⁾ for 12 layers (e.g., Prototype 1).

***Time required while generating a single frequency point in Fig. 10.

methodology and implementation for LLC resonant converters," *IEEE Trans. on Ind. App.*, vol. 52, no. 1, pp. 342–350, 2016.

- (6) P. Raitsios and A. Safacas, "Stromdichte- und Magnetfeldverteilung bei einer Anordnung aus Platten und vielen parallelen Stromleitern," *Archiv für Elektrotechnik*, vol. 75, pp. 411–417, 1992.
- (7) T. Ewald and J. Biela, "Frequency-dependent inductance and winding loss model for gapped foil inductors," *Transactions on Power Electronics*, 2022.
- (8) M. Chen and C. Sullivan, "Unified Models for Coupled Inductors Applied to Multiphase PWM Converters," *IEEE Trans. on Power Electronics*, vol. 36, no. 12, pp. 14 155–14 174, 2021.
- (9) T. Ewald and J. Biela, "Analytical eddy current loss model for foil conductors in gapped cores," in *EPE ECCE Europe*. Ghent: IEEE, 2021.
- (10) D. Leuenberger and J. Biela, "Semi-numerical method for loss-calculation in foil-windings exposed to an air-gap field," in *Int. Power Electronics Conference (IPEC)*. Hiroshima: IEEE, 2014, pp. 868–875.
- (11) T. Ewald and J. Biela, "Analytical winding loss and inductance models for gapped inductors with litz or solid wires," *Transactions on Power Electronics*, 2022.
- (12) C. A. Desoer and E. S. Kuh, *Basic Circuit Theory*. New York: McGraw-Hill, 1969.
- (13) A. J. Hanson and D. J. Perreault, "Modeling the Magnetic Behavior of N-Winding Components: Approaches for Unshackling Switching Superheroes," *IEEE Power Electronics Magazine*, vol. 7, no. 1, pp. 35–45, 2020.
- (14) J. Spreen, "Electrical terminal representation of conductor loss in transformers," *IEEE Transactions on Power Electronics*, vol. 5, no. 4, pp. 424–429, Oct. 1990.
- (15) R. W. Erickson and D. Maksimovic, "A multiple-winding magnetics model having directly measurable parameters," in *PESC Annual IEEE Power Electronics Specialists Conf.* Fukuoka, Japan: IEEE, 1998.
- (16) T. Guillod, F. Krismer, and J. W. Kolar, "Magnetic equivalent circuit of MF transformers: modeling and parameter uncertainties," *Electrical Engineering*, vol. 100, no. 4, pp. 2261–2275, May 2018.
- (17) R. Schlesinger and J. Biela, "Leakage Inductance Modelling of Transformers: Accurate and Fast Models to Scale the Leakage Inductance Per Unit Length," in *EPE ECCE Europe*, Lyon, 2020.
- (18) X. Margueron, A. Besri, P. O. Jeannin, J. P. Keradec, and G. Parent, "Complete analytical calculation of static leakage parameters: A step toward HF transformer optimization," *IEEE Trans. on Industry Applications*, vol. 46, no. 3, pp. 1055–1063, 2010.
- (19) E. Roth, "Étude analytique du champ de fuites des transformateurs et des efforts mécaniques exercés sur les enroulements," *Revue générale de l'électricité*, vol. 23, pp. 773–787, 1928.
- (20) P. Wallmeier, N. Frohleke, and H. Grotstollen, "Improved analytical modeling of conductive losses in gapped high-frequency inductors," in *IEEE Ind. App. Society Conf. (IAS)*, vol. 2, 1998, pp. 913–920.
- (21) R. Schlesinger and J. Biela, "Comparison of Analytical Models of Transformer Leakage Inductance: Accuracy vs. Computational Effort," *IEEE Trans. on Power Electronics*, vol. 36, no. 1, pp. 146–156, 2021.
- (22) *Ferrites and Accessories - SIFERRIT Material N87*, TDK, Sep. 2017.
- (23) A. Roskopf and C. Brunner, "Enhancing litz wire power loss calculations by combining a sparse strand element equivalent circuit method with a voronoi-based geometry model," *IEEE Transactions on Power Electronics*, vol. 37, no. 9, pp. 11 450–11 456, sep 2022.
- (24) K. Niyomsatian, J. J. Gyselinck, and R. V. Sabariego, "Experimental Extraction of Winding Resistance in Litz-Wire Transformers - Influence of Winding Mutual Resistance," *IEEE Trans. on Power Electronics*, vol. 34, no. 7, pp. 6736–6746, 2019.
- (25) J. G. Hayes, N. O'Donovan, M. G. Egan, and T. O'Donnell, "Inductance Characterization of High-Leakage Transformers," in *IEEE App. Power Electronics Conf. and Exp. (APEC)*. IEEE, 2003, pp. 1150–1156.

Thomas Ewald (Non-member) studied electrical engineering with focus on Energy Conversion Technology at Technical University of Munich (TUM) in Germany. He received his B.Sc. and M.Sc. degree from TUM in 2015 and 2018, respectively. In 2017, he wrote his Master's Thesis at BMW AG in the R&D department for electrical drive components. In his Master's thesis he developed an analytical model for simulating transient processes in both, permanent magnet and electrically excited synchronous machines. Since November 2019 he is a Ph.D. student at the Laboratory for High Power Electronic Systems (HPE) at ETH Zurich, working on analytical inductor models and automated optimization processes.



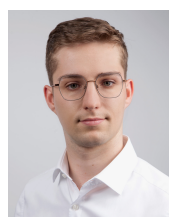
he is a Ph.D. student at the Laboratory for High Power Electronic Systems (HPE) at ETH Zurich, working on analytical inductor models and automated optimization processes.

Richard Schlesinger (Non-member) is pursuing his PhD degree at the Laboratory for High Power Electronic Systems at ETH Zurich since 2018. His research interests include modelling and design of magnetic components with special focus on analytical modelling of the transformer leakage inductance. Richard received the Dipl.-Ing. degree (MSc equivalent) with distinction from TU Wien, Austria in energy and environmental technology in 2018. In his master's thesis he modelled and evaluated three-terminal impedance measurement setups for solid oxide fuel cell electrodes. During his studies, he spent exchange semesters at the UPC in Barcelona and at Beuth UAS in Berlin and worked with the Austrian Institute of Technology.



and evaluated three-terminal impedance measurement setups for solid oxide fuel cell electrodes. During his studies, he spent exchange semesters at the UPC in Barcelona and at Beuth UAS in Berlin and worked with the Austrian Institute of Technology.

Jan P. Agner (Non-member) received his B.Sc. degree in electrical engineering from RWTH Aachen University in 2019. Currently, he is studying electrical engineering at ETH Zurich in Switzerland. He will complete his studies with an M.Sc. degree in 2022. During his master's thesis, he focused on the analytical lumped parameter calculation of gapped multiwinding inductors. In an industry internship, he worked for Dr. Ing. h.c. Porsche AG in the series development of the traction inverter. His interests furthermore include control and optimization of LLC converters and thermal design. He looks forward to starting to work in the automotive industry in September 2022.



and optimization of LLC converters and thermal design. He looks forward to starting to work in the automotive industry in September 2022.

Jürgen Biela (Non-member) received the Diploma (hons.) degree from Friedrich-Alexander Universität Erlangen-Nürnberg, Erlangen, Germany, in 1999, and the Ph.D. degree from the Swiss Federal Institute of Technology (ETH), Zürich, Switzerland, in 2006. In 2000, he joined the Research Department, Siemens A&D, Erlangen, and in 2002, he joined the Power Electronic Systems Laboratory, ETH Zürich, as a Ph.D. Student focusing on electromagnetically integrated resonant converters, where he was a Postdoctoral Fellow from 2006 to 2010. Since 2010, he has been an Associate Professor, and since 2020, a Full Professor of high-power electronic systems with ETH Zurich.



2006 to 2010. Since 2010, he has been an Associate Professor, and since 2020, a Full Professor of high-power electronic systems with ETH Zurich.